Int. J. Electrochem. Sci., 15 **(2020)** 4602 – 4618, doi: 10.20964/2020.05.72

International Journal of ELECTROCHEMICAL SCIENCE
www.electrochemsci.org

Electrospinning Preparation of Fe_3O_4/Porous Carbon Nanofibres for use as Supercapacitor Electrode Materials

Xia Jiang[1,2], *Gaofeng Shi*[*,1], *Guoying Wang*[*,1], Puranjan Mishra[3], *Zhao Wang*[1], *Qi Zhang*, *Hongquan Zhang*[1], *Xiuli Niu*[*,4]

[1] School of Petrochemical Engineering, Lanzhou University of Technology, Lanzhou city, China
[2] Gansu Vocational College of Agriculture, Lanzhou city, China
[3] Faculty of Engineering Technology, Universiti Malaysia Pahang, Lebuhraya Tun Razak, 26300 Gambang, Kuantan, Pahang, Malaysia
[4] Gansu Province Food Inspection Institute, Lanzhou city, China
[*]E-mail: gaofengshi_lzh@163.com , wangguoying@lut.edu.cn

Received: 30 Janaury 2020 / *Accepted:* 2 March 2020 / *Published:* 10 April 2020

A Fe_3O_4/porous carbon nanofibre (Fe_3O_4/CNF) was prepared by carbonization of electrospun polyacrylonitrile (PAN)/polymethylmethacrylate (PMMA) composite nanofibres and used as electrode materials for supercapacitors. The introduction of PMMA as a pore- forming agent in PAN results in an optimum pore distribution and a more suitable specific surface area for Fe_3O_4/CNF; the improved pores and surface area contribute to the diffusion of the electrolyte from the surface to the inside of the electrode material. Electrochemical measurements of the Fe_3O_4/CNF in three- and two- electrode systems reveal a maximum specific capacitance of 540 F g^{-1} in the three-electrode system and a capacitance retention of 76.3 % after 5000 continuous cycles in the two-electrode system. Due to the synergistic effect of redox pseudocapacitance behaviour and bilayer capacitance, the excellent electrochemical performance of the Fe_3O_4/CNF electrode highlights the importance of adding PMMA into composite materials.

Keywords: iron oxide; carbon nanofibers; pore structure; liquefied carbon; supercapacitors

1. INTRODUCTION

Supercapacitor is a new type of energy storage device with great advantages, including fast charge discharge rate, excellent cycle stability and high power density [1-3]. Generally, the development of appropriate electrode materials is the main challenge for the development of high-performance supercapacitors. At present, the main electrode materials of supercapacitors have been studied as carbon materials, transition metal compounds and conductive polymers [4-6]. Carbon (graphene, activated carbon, carbon nanofibers, etc.) is used as the material of double layer capacitors, while transition metal oxides and conductive polymers are used as the pseudo capacitor material [7-

10]. The carbon materials have stable electrochemical performance, good electrical conductivity, low capacity, and low energy density. The electrode materials of the pseudocapacitors have large specific capacitance, which increases the energy density of the capacitor. However, their cycle stabilities are relatively poor, and they are prone to structural collapse [11-13]. Therefore, carbon materials are used as carrier materials to appropriately dope the metal oxide, which can effectively enhance the mass ratio capacitance, capacity and cycle stability of the electrode, so that the electrode materials of the pseudocapacitor are greatly improved.

Therefore, we find that the high surface area and porosity of the electrode material are very important to enhance the specific capacitance and cycling stability of the capacitor to achieve high performance. Ui Guo et al. [14] reported activated activated textile carbon as a flexible material to grow $CoNiO_2$, which effectively improved the capacity and cycle stability of the electrode, thereby greatly improving the performance of the electrode material of the pseudocapacitance. Jiaxin Ma et al. [15] reported that the sheet metal organic framework was directly grown on the carbon cloth of textiles as the electrode of high-performance supercapacitor, which also improved the electrochemical performance. Do Geum Lee [16] used polymethyl methacrylate as the electrode of electrochemical capacitor, and prepared porous MnO_2/carbon nanofiber composite with hollow core by simple electrospinning method. This method increases the specific capacitance of electrode material.

Among various metal oxide electrode materials for supercapacitors, iron oxides have also been found to exhibit comparable capacity in capacitor applications. Because of its large theoretical capacity (3625 F g^{-1}), rich in nature, cheap and easy to obtain, environmentally friendly and harmless, it is beneficial to its practical application in energy storage devices [17]. Unfortunately, as pseudocapacitor electrode material, iron oxide has the disadvantages of high contact resistance and insufficient capacitance display due to its inherent low conductivity and lack of accessible surface area [18-20]. Therefore, due to the synergistic effect of double layer capacitor and pseudocapacitor, this disadvantage can be overcome by using high conductivity carbon material as the carrier material of iron oxide, so as to improve the efficiency and stability of charge exchange during the redox cycle of iron oxide electrode.

In this work, a one-step method was developed to prepare porous carbon nanofibers with controllable iron oxide/porous structure for pseudocapacitor electrodes. Carbon nanofibers were prepared by electrospinning PAN/PMMA mixture with different mass rotios, followed by further high temperature carbonization to obtain porous carbon nanofibers. In the carbonization process, PAN is a carbon source for forming carbon nanofibers, and the complete decomposition of PMMA produces uniform pores in the carbon nanofibers [21, 22]. The porous structure of the carbon nanofibers can be controlled by adjusting the weight ratio of PAN to PMMA. In addition, iron acetylacetonate ($Fe(acac)_3$) was added as an iron oxide precursor to the PAN/PMMA mixture. The additional inner surface and micropores or mesopores increase the specific surface area and pore volume compared to conventional electrospun carbon nanofibers, which facilitates the diffusion of electrolyte from the outside into the interior of the electrode material, resulting in rapid ion transport, which is very advantageous for enhancing the electrochemical capacitance. Morphological and electrochemical characterization of the composites revealed that they exhibited good electrochemical properties. In order to increase the application of biomass materials in electrospinning, the hemp straw is converted into liquefied carbon by lignin liquefaction, and then doping into PAN as an electrospinning precursor liquid [23-25]. This method opens up the application of biomass materials in electrospinning. The entire preparation process is shown in Figure 1.

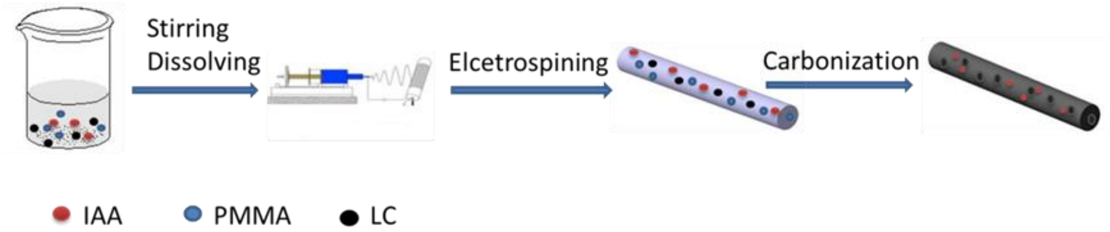

Figure 1. Schematic diagram of preparation of the FePMCNF-X.

2. EXPERIMENTAL

2.1 Chemicals and Reagents

All chemicals used in this work were of analytical reagent (AR) grade. Hemp straw was purchased from Gansu Province, China. The polyacrylonitrile [PAN], N, N-dimethylformamide [DMF], Polymethylmethacrylate [PMMA], iron(III) acetylacetonate ($Fe(acac)_3$) [IAA] were purchased from Chemical Reagent Co., Ltd. and no further processing. Deionized water (purified by Millipore-Q System) was used throughout the experiment.

2.2 Experimental details

First, the hemp straw was prepared into liquefied carbon by liquefaction technology. The specific method refers to our previous research [26]. In brief, the hemp straw was crushed to the powder. Then, with 10% phosphoric acid as catalyst, hemp powder and phenol were mixed at a mass ratio of 1: 5 and liquefied at 160 °C. The wood phenol liquefied material was obtained afterward. We converted lignin into liquefied carbon and incorporated it into PAN as a precursor of electrospinning (PAN - LC) according to PAN : liquefied carbon = 9 : 1. In DMF solution, the appropriate amount of IAA (3 wt%) was dispersed into PMMA/PAN-LC with different mixing ratio to prepare electrospinning solution. Mixed continuously at 60 °C and cooled to room temperature. Nanofibers are produced using electrospinning equipment (Beijing Yongkang Liye). The precursor solution was added to a syringe with a stainless steel needle. For electrospinning, the positive high voltage is 15 kV and the negative high voltage is -2 kV. The distance between the current collector and the nozzle is fixed at 15 cm, the flow rate is 0.13 mm min^{-1}, during this process, the ambient temperature is 25 °C.

The as-spun nanofibers were collected and stabilized in a convection oven at 280 °C for 1 h in air. Finally, by comparing the morphology and electrochemical properties, we screened the carbonization temperature to 800 °C (from Figure s2-s3). These stabilized nanofiber mats were carbonized at 800 °C for 1 h with a heating ramp rate of 2 °C min^{-1} under a constant flow of nitrogen gas to synthesize Fe_3O_4/CNF. The sample was named as FePMCNF-X, where X (x = 0, 1, 2 or 3) stands for the different mass ratio of the PMMA : PAN - LC (1 : 0, 9 : 1, 8 : 2, 7 : 3).

2.3 Structure characterization

The morphology and microstructures were characterized by scanning electron microscopy (SEM, JSM-6701F, Japan), High resolution HRTEM (JEOL JEM 2100) and Transmission electron microscope (TEM) units. The X-ray photoelectron spectra (XPS, PHI5702, USA) was used to confirm binding energies. Raman spectrum was measured by using the Jobin Yvon HoribraLABRAM - HR visible spectrometer with an argon ion continuous wave laser (532 nm) as the excitation source. The specific surface area was used by volumetric sorption analyzer (BET micromeritics ASAP 2020).

2.4 Test of electrochemical properties

The electrochemical measurements were carried out on a CHI660E electrochemical workstation (Shanghai Chenhua instrument Co., Ltd.). In the three electrode system, platinum foil was used as the counter electrode, Hg/HgO electrode as the reference electrode and 6 M KOH solution as the electrolyte.

FePMCNF-X material, acetylene black and polyvinylidene fluoride (PTFE) were mixed in ethanol at a mass ratio of 85 : 10 : 5 to prepare slurry. Then the slurry was loaded onto nickel foam (2 cm × 1 cm) and dried at 70 °C for 12 h, then pressed at 8 MPa to prepare the working electrode.

For a three electrode configuration, specific capacitance of the electrode materials was calculated by Eq. (1):

$$C = \frac{I\Delta t}{m\Delta V} \quad (1)$$

Where I refers discharge current (A), Δt refers discharge time (s), m refers the mass of electrode (g), and ΔV refers voltage window (V).

In the two electrode system, the fabricated FePMCNF-X was used as the electrode material to assemble the symmetrical super capacitor battery. The membrane (PP/PE composite membrane), 6 M KOH electrolyte and FePMCNF-X electrode were assembled into symmetrical electrode/membrane/ electrode structure. Cyclic voltammetry (CV), constant current charge discharge (GCD) and impedance (EIS) were tested on a chi660E electrochemical workstation. The cycle stability was tested by the computer-controlled supercapacitor test system (neware 5v0.1a, Shenzhen, China).

Calculating the mass ratio of the supercapacitor for the two-electrode condition by Eq. (2):

$$C = \frac{I\Delta t}{2m\Delta u} \quad (2)$$

Where Δt is the discharge time, I is the discharge current, m is the mass of the working electrode, and Δu is the voltage variation range.

3. RESULT AND DISCUSSION

3.1 Structural characterization

According to the literature reports [27, 28], PMMA begins to decompose at 200 °C, and completely decomposes at approximately 360 °C, and then it is completely converted into volatile products and released. In the carbonization process, when the temperature is higher than 360 °C, PMMA will be completely pyrolyzed and pores will be generated in situ. Therefore, we analyzed the composite nanofiber membrane FePMCNF-a after electrospinning by thermogravimetry. The thermogravimetric curve is shown in Figure 2. We can see that under the condition of N_2 protection, the temperature of FePMCNF-a decreases sharply between 260 °C and 400 °C. Therefore, we can conclude that in FePMCNF-X material, due to the incompatibility between PAN and PMMA materials, while PAN is used as a carbon scaffold for metal oxide fibers during high-temperature carbonization, PMMA as a sacrificial phase generates a randomly dispersed pore structure in PAN after complete thermal decomposition, the resultant pore structures help the material to have a large specific surface area and high porosity, thereby improving the electrochemical performance of the material.

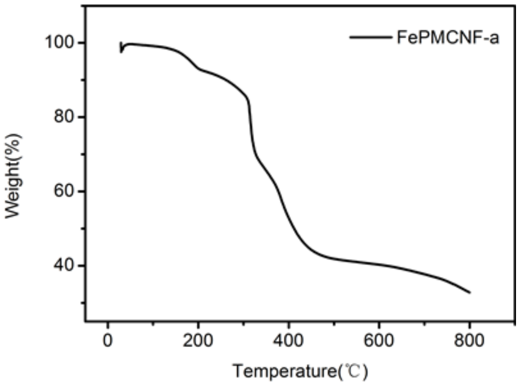

Figure 2. TGA curves of the FePMCNF-a.

The morphological and structural features of the FePMCNF-X nanocomposites were characterized by SEM, TEM, and HRTEM. As can be seen in Figure 3, the morphology of the nanofibers obtained from neat PAN (FePMCNF-0) and the PAN/PMMA (FePMCNF-1, FePMCNF-2 and FePMCNF-3). The FePMCNF-0 composites from pure PAN have smooth surface and no obvious holes (Figure 3a), while FePMCNF-1, FePMCNF-2 and FePMCNF-3 (Figure 3b-3d) of the porous carbon nanofibers become rougher and some nanofibers are bonded together. After the formation of the electrospun carbon nanofibers (Figure 3e), and after the preoxidation (Figure 3f), the carbon nanofibers maintain a smooth morphology, but after calcination at 800 °C, a rough surface is formed. The formation of such rough surface should be attributed to the formation of cavities and holes originating from the release of volatile products by the decomposition of PMMA at high temperature.

Therefore, we conclude that the addition of PMMA has a certain pore-forming effect on porous carbon nanofiber materials.

Figure 4a shows the TEM images of the FePMCNF-2. We can see that the surface of the FePMCNF-2 material is rough and has obvious holes, which is consistent with the SEM results. It can also be clearly seen that Fe_3O_4 nanoparticles are evenly embedded on the surface of carbon fiber. Furthermore, the HRTEM image of the FePMCNF-2 composite (Figure 4b) shows a lattice spacing of 0.25 nm, corresponding to the (311) plane of cubic phase Fe_3O_4 [29], which reveals that the Fe_3O_4 is well crystallized, which is in agreement with the XPS results (see below). The SAED pattern of the selected area (Fig. 4C) also shows that the FePMCNF-2 is highly crystalline. Figures 4d-4g show an EDX mapping image showing a uniform distribution of C, O, N and Fe elements in FePMCNF-2. It is further confirmed that Fe_3O_4 nanoparticles are uniformly dispersed in the carbon skeleton. We introduce liquefied carbon from hemp straw into PAN as precursor liquid for electrospinning. It is a kind of biomass materials. Clearly, the N comes from hemp straw and PAN.

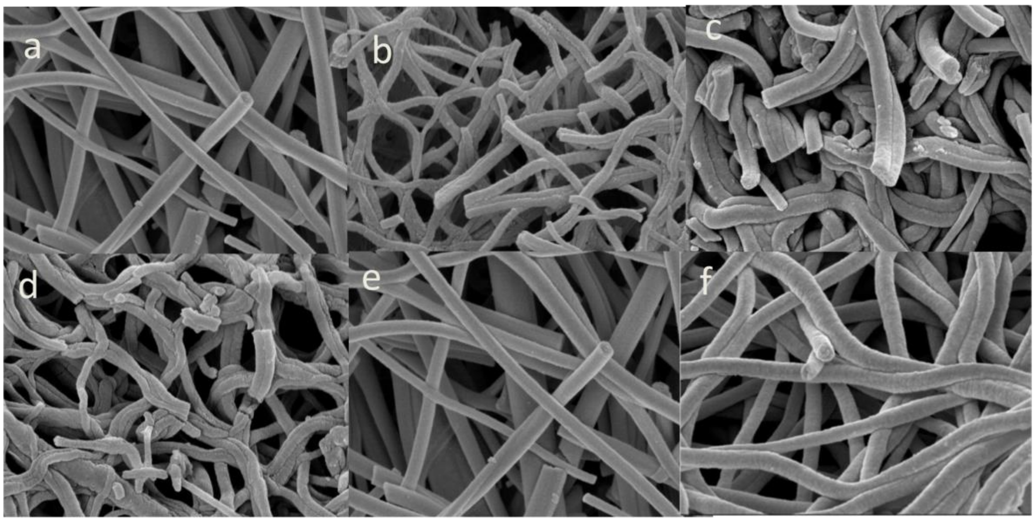

Figure 3. SEM images of (a) FePMCNF-0, (b) FePMCNF-1, (c) FePMCNF-2, (d) FePMCNF-3, (e) Electrospinning of FePMCNF-2, (f) Pre-oxidized of the FePMCNF-2.

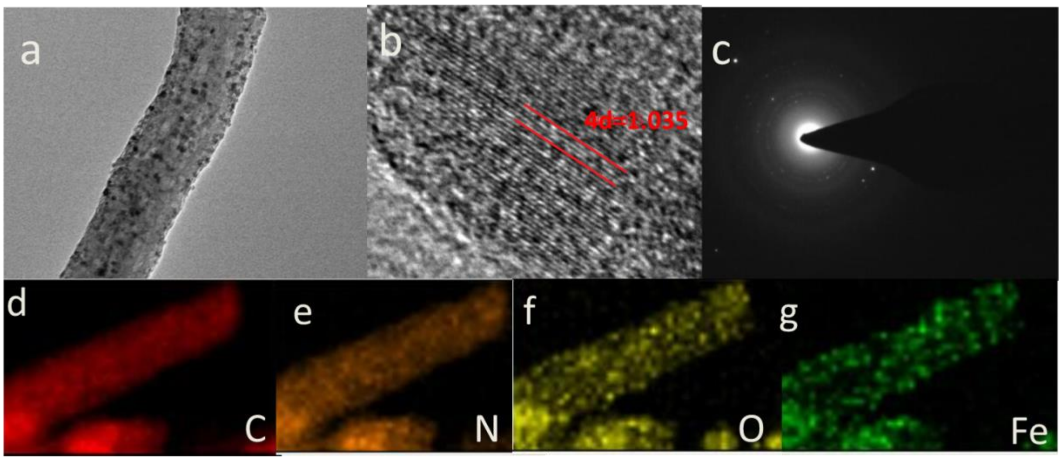

Figure 4. TEM images of (a) a single of the FePMCNF-2, (b) the HRTEM image of the FePMCNF-2, (c) The SAED pattern of the FePMCNF-2, (d -g) FePMCNF-2 EDX element mappings.

Nitrogen adsorption - desorption isotherms and the pore size distribution for the FePMCNF-X measurements are shown in Figure 5a and 5b. The adsorption desorption isotherms of nitrogen all show IV type adsorption isotherms, indicating that the materials have uniform microporous and mesoporous structures. According to Table 1, we can find that compared with FePMCNF-0, with the addition of PMMA, the specific surface area of FePMCNF-X is gradually increased, and FePMCNF-3 has the highest specific surface area. According to the electrochemical charge storage mechanism of supercapacitors, the capacitance of carbon materials has a direct relationship with their specific surface area, but there is not always a linear relationship between them. In contrast, many materials with a large specific surface area and high porosity do not show better specific capacitance [30]. Generally, in carbon materials, the large pores provide an electrolyte storage location to reduce the distance between the interface and the inner surface. The mesopores provide a fast channel for electrolyte transfer, and the micropores have conductivity, which further improves the super capacitor Specific capacitance [31, 32]. Hence, micropores and mesopores in the proper ratio will show good electrochemical performance. Through the later electrochemical performance test (see below), it shows that FePMCNF-2 has the best electrochemical performance, so the FePMCNF-2 have the best pore distribution ratio (meso/micro = 0.834).

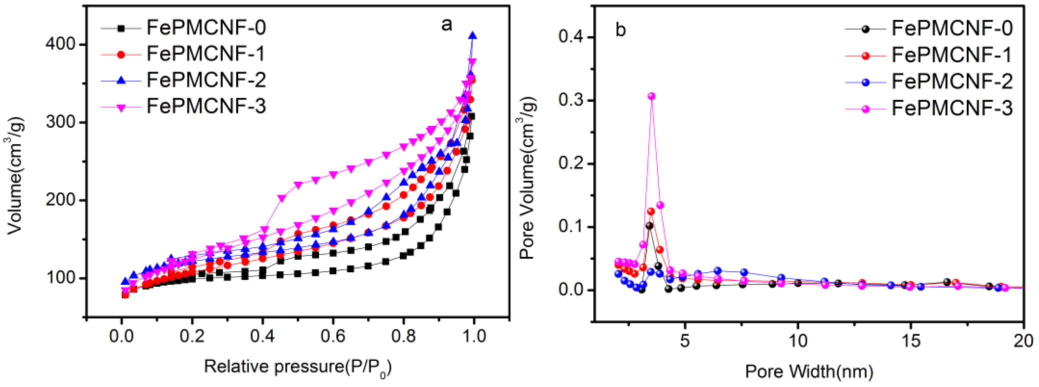

Figure 5. (a) N_2 adsorption/desorption isotherms of samples (b) Pore size distributions of samples.

Table 1. Surface area and pore volume of samples.

	Surface area(m^2/g)	Total pore Volume(cm^3/g)	S_{micro} (cm^2/g)	S_{meso} (cm^2/g)	Meso / micro ratio
FePMCNF-0	337.99	0.371	225.314	112.681	0.500
FePMCNF-1	377.27	0.451	135.807	241.464	1.778
FePMCNF-2	420.26	0.469	229.262	191.001	0.834
FePMCNF-3	440.82	0.507	91.276	349.544	3.830

X-ray diffraction (XRD) and Raman analyses were performed with the FePMCNF-X materials. The XRD analysis in Figure 6a shows that all materials contain diffraction peaks that correspond well to Fe_3O_4 (JCPDS card number 3-863), along with the presence of the typical carbon diffraction peaks for the (002) and (100) lattice planes of graphitic carbon at 25° and 43° [33, 34]. However, due to the low Fe content (as can be seen in the XPS analysis later), the peak of Fe3O4 is not obvious. But we can still see faint peaks.In the Raman analysis of Figure 6a, we can clearly see the G and D peaks of the carbon material. The D band represents the disordered carbon structure, and the G band is related to the sp^2 hybrid carbon in the graphite structure [35]. The intensity ratio (I_D/I_G) between D-band and G-band is used to indicate the degree of graphitization [36], and the I_D/I_G of FePMCNF-0, FePMCNF-1, FePMCNF-2, and FePMCNF-3 are calculated by 1.16, 1.18, 1.20, and 1.19. The results show that FePMCNF-1, FePMCNF-2 and FePMCNF-3 have a higher degree of graphitization than FePMCNF-0. After doping PMMA, more defects were introduced into the structure and the structure will be more disordered, which will provide more electrochemical reaction sites. In addition to the obvious D and G peaks for carbon nanofibers, it is clear that the peaks at 219 and 290 cm^{-1} are due to the vibrational bands of the T_{2g} and E_g modes of Fe_3O_4 [37], respectively. This is in line with the above High-resolution TEM (HRTEM) and further illustrates that the sample contains Fe_3O_4. The analysis of the XRD and Raman spectra showed that the Fe_3O_4 carbon nanofiber composite was successfully prepared and further confirms the structure of FePMCNF-Xs.

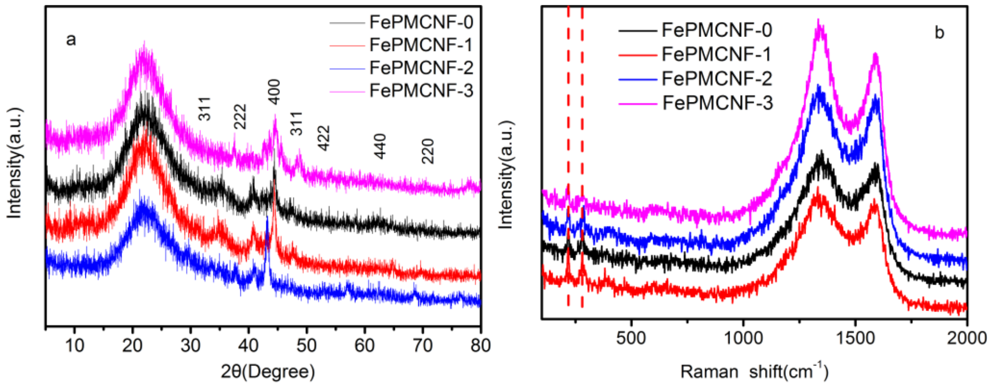

Figure 6. (a) XRD patterns for the FePMCNF-Xs, (b) Raman spectra of the FePMCNF-Xs.

In order to analyze the chemical bonding states of the C, O, and Fe elements in theFePMCNF-2 composite, we performed XPS characterization on the FePMCNF-2. The XPS spectra of FePMCNF-2 shows four distinct peaks, which are well attributed to C, N, O and Fe atoms, as shown in Figure 7a. The XPS analysis revealed that the proportions of C, N, O, and Fe elements in FePMCNF-2 were 89.0 2%, 2.45%, 6.77%, and 1.76% (atomic%), respectively. Through the carbonization process, the N element in PAN and liquefied carbon can be partially converted into FePMCNF-Xs. This is consistent with EDX mapping. The presence of N element can achieve in-situ doping of N element, which plays a positive role in the electrochemical performance of the material.

The C 1s spectrum exhibits mainly two peaks (as shown in Figure 7b), which located at 284.6 and 285.7 eV, corresponding to C-C sp^2， C-C sp^3 [38, 39]. Figure 7c displays that the N 1s spectrum of FePMCNF-2 can fit well with pyridinic N (N-6), pyrrolic N (N-5) and quaternary N (N-Q), which peaks at 398.61, 400.73, and 401.11 eV, respectively. Generally, the pryidinc N and graphitic N have electroactive sites, which would benefit the enhancement of electrical conductivity and capacitance[40]. The O 1s spectrum shown in Figure 7d, the bands at 530.24, 531.86 and 533.48 eV can be attributed to the oxygen bond of Fe-O, Fe-O-H and H-O-H, respectively [41-43]. In the Fe 2p XPS spectrum shown in Figure 7e, the element Fe displays photoelectron peaks at 710.23 and 723.61

eV, which can be indexed to Fe $2p_{3/2}$ (Fe_3O_4), and Fe $2p_{1/2}$ (Fe_3O_4). These results indicate that iron oxide particles are present in the form of F_3O_4 [44, 34]. All the results indicate the synthesized sample is Fe_3O_4/CNF composite.

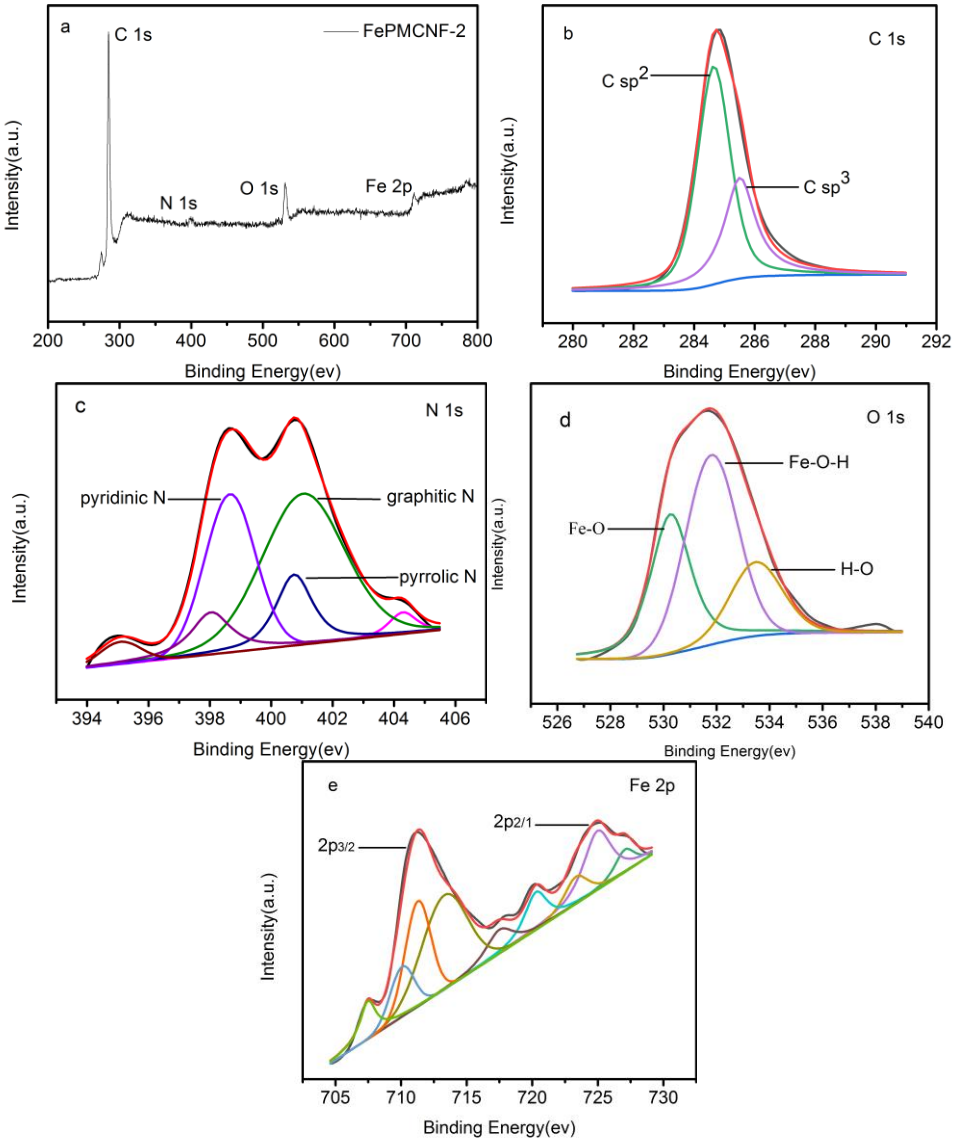

Figure 7. (a) XPS spectrum, (b) C 1s high - resolution spectrum, (c)N 1s high - resolution spectrum, (d) O 1s high-resolution, (e)Fe 2p high - resolution spectrum of the FePMCNF-2.

3.2 Electrochemical characterization

Due to the excellent structural advantages, FePMCNF-X materials are expected to demonstrate good electrochemical performance. The electronic performance of FePMCNF-Xs electrodes were first evaluated in three - electrode system with 6 M KOH as the electrolyte. Figure 8a shows the CV curves of four different FePMCNF-Xs between -1.2 V to - 0.4 V at 10 mV s^{-1}. All samples show typical pseudocapacitive behavior with prominent oxidation and reduction peaks, and FePMCNF-2 has the largest CV - circulated areas, thus it has the highest capacitance among all four materials. Moreover, we clearly see that after the addition of PMMA as a pore forming agent, the pore structure of the material changes, and the CV - circulated area of FePMCNF-1, FePMCNF-2 and FePMCNF-3 are much larger than that of FePMCNF-0, thus, their performance as capacitors has been greatly improved. Figure 8b shows the CV curves of FePMCNF-2 at different scan rates from 5 m V s^{-1} to 50 m V s^{-1} in the potential window from -1.2 V to -0.4 V. It can be observed that all CV curves have obvious redox peaks, whose positions move from lower scanning rate to higher scanning rate. Furthermore, the redox peak in CV curve represents the typical pseudo capacitance behavior.

The GCD curves of the FePMCNF-Xs under the current density of 1 A g^{-1} and the potential window of -1.1 V to 0 V, all show asymmetric shape, and the deviation from the linear GCD curve confirms the existence of pseudo capacitance (Figure 8c). They also show that the discharging time for FePMCNF-2 is much longer than those for FePMCNF-0, FePMCNF-1 and FePMCNF-3, which indicates the higher capacitance of the FePMCNF-2 and is consistent with the CV. According to Eq. (1), the calculated specific capacitances in terms of the charge-discharge curves are 414, 450, 540 and 501 F g^{-1} for FePMCNF-0, FePMCNF-1, FePMCNF-2 and FePMCNF-3, respectively. The GCD curves of FePMCNF-2 at different current density from 1 A g^{-1} to 20 A g^{-1} are shown in Figure 8d. For all these current densities, the GCD curves of FePMCNF-2 show asymmetrical shapes indicating the presence of pseudocapacitance behaviour .

The fast ion diffusion behaviour of the FePMCNF-Xs is also reflected in their EIS analysis. The impedance spectrum consists of a low frequency vertical line and a high frequency quasi-circular circle. As shown in Figure 8e, the almost straight line indicates the diffusion resistance and mass transfer rate of the electrolyte in the electrode pores [45]. It can be clearly seen that the increase in PMMA improves the pore structure of the material and leads to a linear increase in slope.

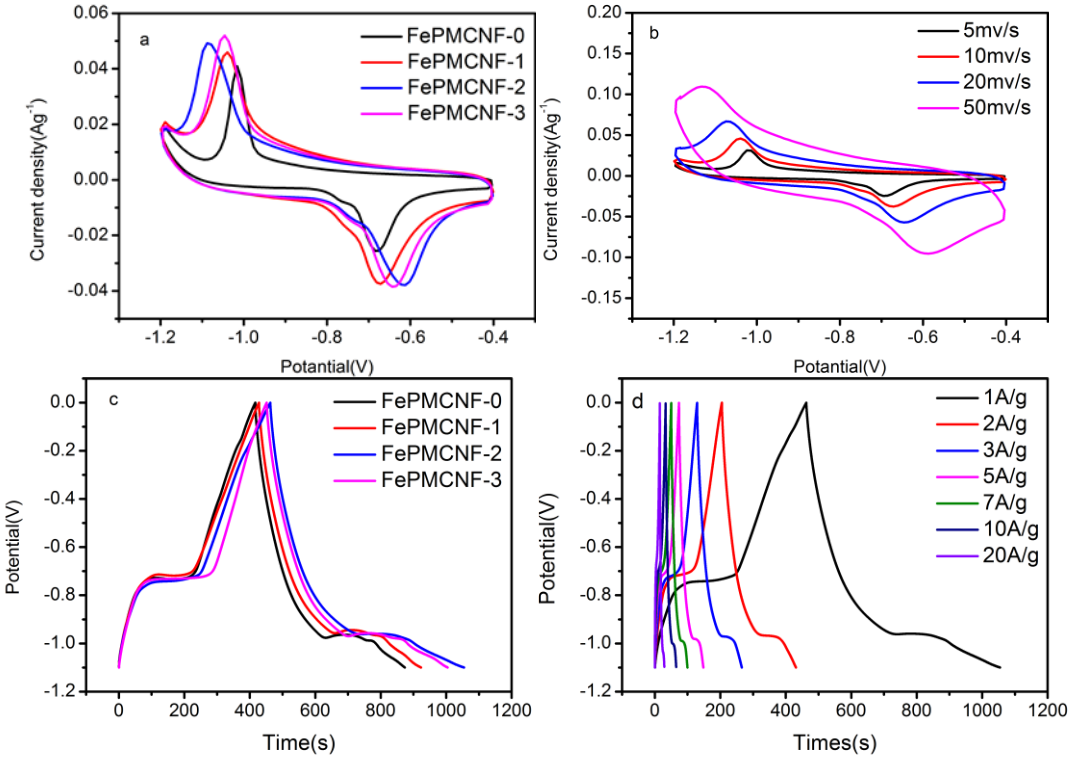

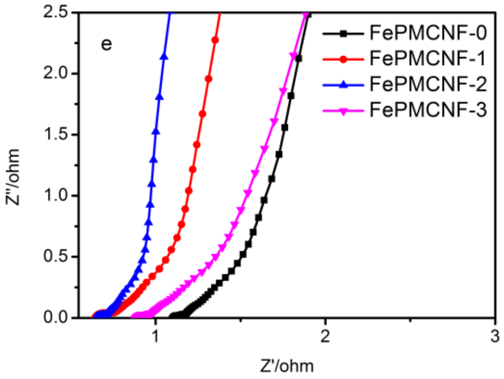

Figure 8. Electrochemical evaluation of the FePMCNF-Xs in three electrode system. (a) CV curves for the FePMCNF-Xs at a scan rate of 10 mv s^{-1}; (b) CV curves for the FePMCNF-2 at scan rates ranging from 5 to 50 mV s^{-1}; (c) GCD curves of FePMCNF-Xs at the current density of 1 A g^{-1}; (d) GCD curves of the FePMCNF-2 at different current densities; (e) EIS of the FePMCNF-Xs.

To demonstrate the superior capacitive performance of the FePMCNF-X electrode, we built a symmetric capacitor device by using the FePMCNF-X as symmetric electrode (denoted as FePMCNF-X//FePMCNF-X). Before the testing, we have selected the best voltage range for the symmetric capacitor batteries (Figure S1). The CV curves are shown in Figure 9a and 9b. They demonstrate that the symmetric capacitor devices show excellent capacitive behavior between 0 V - 1.1 V. Furthermore, the almost symmetric GCD curves (Figure 9c, 9d) indicate a high coulombic efficiency and electrochemical reversibility. According to Eq. (2), the specific capacitances of the symmetric capacitor devices are calculated to be 149, 174, 189 and 181 F g^{-1} at current density of 1 A g^{-1} for FePMCNF-0, FePMCNF-1, FePMCNF-2 and FePMCNF-3, respectively. We can still see that as the symmetric capacitor device batteries, the performance of the electrode material with the introduction of PMMA exhibits superior electrochemical performance, especially the FePMCNF-2, which has the best capacitance performance. This is also consistent with the previous structural analysis, which has the best pore distribution.

Figure 9e displays the specific capacitances of the devices of the FePMCNF-Xs at different current densities (1, 2, 3, 5, 7, 10, and 20 A g^{-1}). We can see that the FePMCNF-2 battery has the highest specific capacitance and a specific capacitance retention rate of up to 74.1 %, which means maintains excellent stability throughout the charge - discharge test. It is clear that the FePMCNF-2 battery has better rate characteristics. This further confirms that the optimal pore distribution structure facilitates ion diffusion and migration at high current densities.

The Nyquist plots for symmetric capacitor batteries are shown in Figure 8f, the straight line which tends to be almost vertical represents the diffusion resistance and mass transfer rate of electrolyte in the electrode hole [46], and it is clearly that with increasing PMMA concentration the slope the slope linearly increases, and FePMCNF-2 has the largest linear slope. The R_f of FePMCNF-0, FePMCNF-1, FePMCNF-2 and FePMCNF-3 electrodes are calculated to be 1.1, 0.47, 0.45 and 0.51 Ω, respectively. Therefore, owing to its small charge transfer resistance and low diffusion resistance, the FePMCNF-2 electrodes can be supposed to facilitate an improvement to the accessibility of ions at the pore surface, thus enhancing ion transportation in the channels.

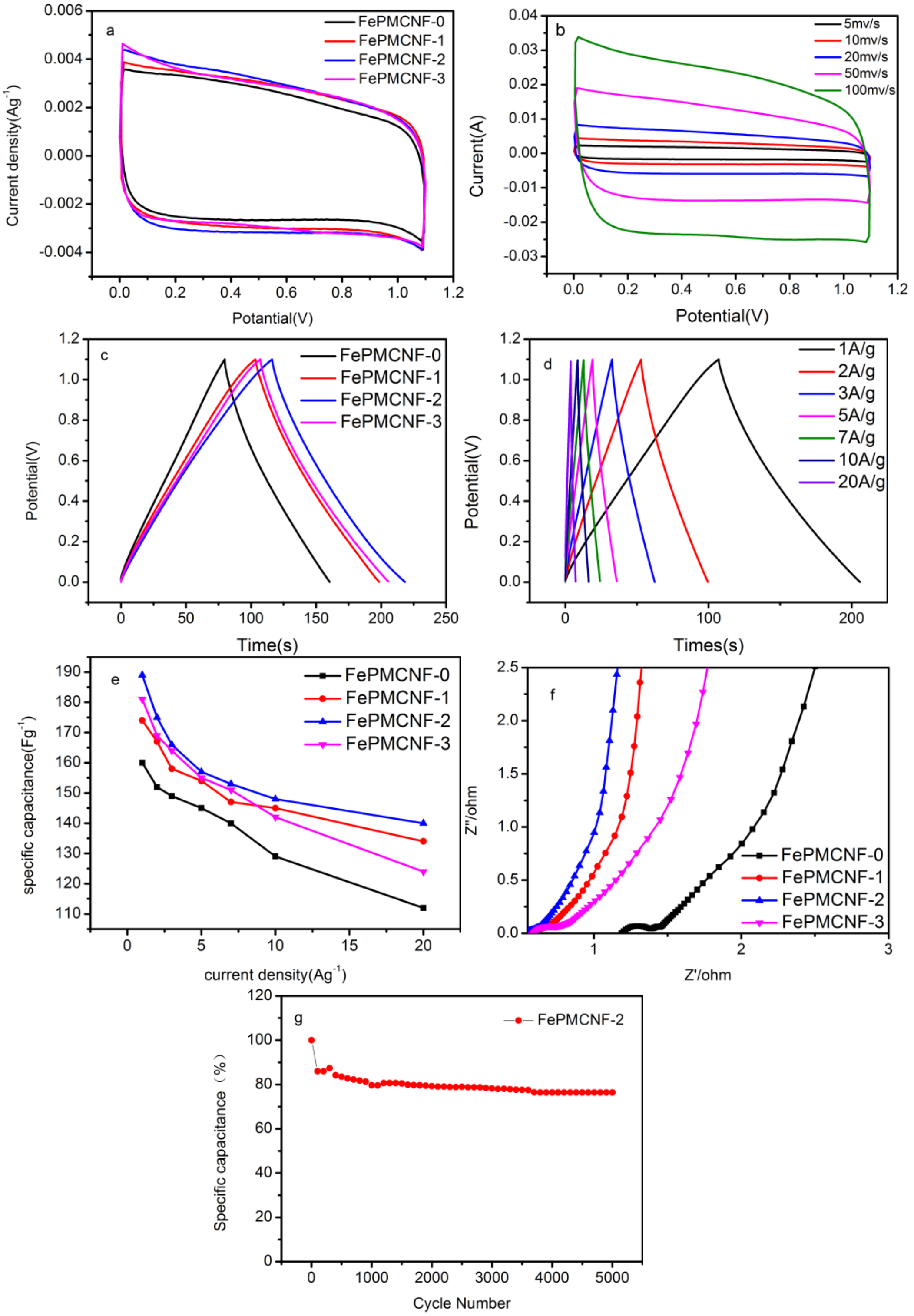

Figure 9. Electrochemical performance of the samples measured in the two electrode system as the symmetric capacitor device. (a) CV curves for FePMCNF-Xs at scan rate of 10 mv s^{-1}; (b) CV curves for the FePMCNF-2 at scan rates ranging from 5 to 100 mV s^{-1}; (c) GCD curves FePMCNF-Xs at the current density of 1 A g^{-1}; (d) GCD curves of the FePMCNF-2 at different current densities; (e) Specific capacitance of the samples versus various current densities from 1 to 20 A g^{-1}; (f) EIS of the FePMCNF-Xs; (g) Cycling stability performance of the FePMCNF-2-based capacitor device at the current density of 2 A g^{-1} after 5000 cycles.

Figure 9g shows the cycling performance of the FePMCNF-2-based capacitor device at constant current density of 2 A g^{-1}. It exhibits outstanding cycling stability with a capacitance retention of 76.3 % after 5000 continuous cycles. This conclusion clearly shows that FePMCNF-2-based capacitor can maintain almost the same ion and electron transport properties in the long-term cycle. These characteristics are very important for the practical application of the FePMCNF-2 electrode in electrochemical energy storage.

Nimali C. Abeykoon [48] and Guanghua He [27] prepared PAN/PMMA composite nanofibers by electrospinning and used them as electrode materials for double layer supercapacitors; then, they studied their capacitance properties. Both of them showed high cycling stability and low specific capacitance. Do Geum Lee [16] doped MnO_2 in a PAN/PMMA polymer to prepare hierarchical porous MnO_2/CNF composites as electrode materials for electrode materials with pseudocapacitance behaviour. Compared with the pure PAN/PMMA polymer, the performance was greatly improved. At present, there is no literature report on the application of PAN/PMMA polymers with carbon nanofibers of iron-based compounds, so our work has prepared Fe_3O_4/porous carbon nanofibers for the first time. Compared with the abovementioned results, our material exhibits better capacitor performance. When the current density is 1 A g^{-1}, the specific capacitance is as high as 540 F g^{-1}, and it has similar cycling stability at a current density of 2 A g^{-1}. At the same time, doping with bio-based liquefied carbon greatly reduces production costs.

Table 2. Comparison of electrochemical performance of some nanofiber electrodes.

Electrode materials	Specific capacitance (Current density or scan rate)	Specific capacitance retention(cyclic times)	Electrolyte	Referencces
PAN/PMMA polymer carbon nanofiber	140 F g^{-1}(-2.0 - 2.0 V, 10 mV s^{-1})	85% (1000)	Three-electrode system	[47]
PAN/PMMA composite nanofibers	140 F g^{-1} (0.5 A g^{-1})	95.4% (1000)	Two-electrode system	[27]
Hierarchical porous MnO_2/carbon nanofiber composites	228 Fg^{-1} (1mA cm^2)	88 % (1000)	Three-electrode system	[16]
Fe_3O_4/porous Carbon Nanofibers	540 F g^{-1} (1 A g^{-1})	76.3 % (5000)	Three-electrode system	This work

4. CONCLUSIONS

In this study, Fe_3O_4/porous carbon nanofibers were prepared by using PMMA as a pore former. During high temperature carbonization, PMMA decomposes, which results in porous PAN/PMMA carbon nanofibers that have an optimum pore distribution and a large specific surface area. These holes provide a convenient electrolyte channel. The electrochemical performance measurements in three and two electrode systems show that the Fe_3O_4/CNF composite based on PAN : PMMA (8 : 2) has the best electrochemical performance. The excellent electrochemical performance of Fe_3O_4/CNF is mainly attributed to the interaction between Fe_3O_4 and the abundant pores in the carbon nanofibers, which can store energy on the surface of the electrode by a redox reaction and increase the transfer rate of ions into the pores. To increase the application of biomass materials in electrospinning, liquefied carbon which comefrom the hemp straw was introduced into the electrospinning precursor liquid. Our previous research opened up the application of biomass materials in electrospinning. The results show that the combination of PMMA as a poreforming agent, liquefied carbon as a precursor of electrospinning, and an iron doped composite as an energy storage electrode material, has great development potential.

ACKNOWLEDGEMENTS
This work was supported by the National Natural Science Foundation of China [21567015, 21407072]; The National Key R & D Program of China [2016YFC0202900]; The Natural Science Foundation of Gansu Province [17JR5RA109]; The Gansu Provincial Party Committee Young Creative Talents [Ganzutongzi[2017]121]; Gansu Provincial Institutions of Higher Learning Innovation Ability Promotion Project(2019A-220); The Food and Drug Research Project of Gansu Province [2018GSFDA014]; The Hongliu Science Fund for Distinguished Young Scholars (2018); Lanzhou University of Technology Hongliu First-class Discipline Construction Program.

SUPPORTING INFORMATION

The potential window of the assembled FePMCNF-2//FePMCNF-2 battery was detected by CV at a scan rate of 100 m V s^{-1} (Figure S3). From 0.8 V to 1.5 V, a rectangular CV curve can be observed, indicating its typical electric double layer behavior. When the operating voltage of the capacitor is extended to 1.1 V, good symmetry can still be exhibited. When the operating voltage continues to increase, a water electrolysis reaction occurs, and gas is precipitated, thereby affecting the performance of the capacitor. Therefore, 1.1 V may be a good choice.

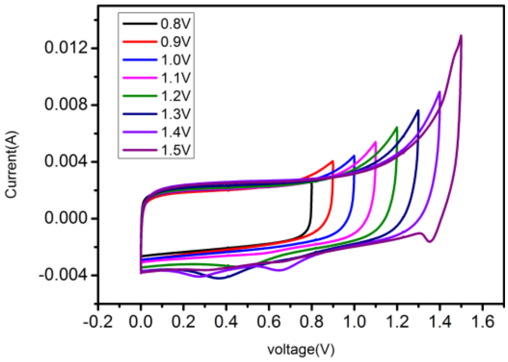

Figure S1. CV curves of symmetric electrode (denoted as FePMCNF-2//FePMCNF-2) cells measured at different potential window at a scan rate of 10 mV s^{-1}.

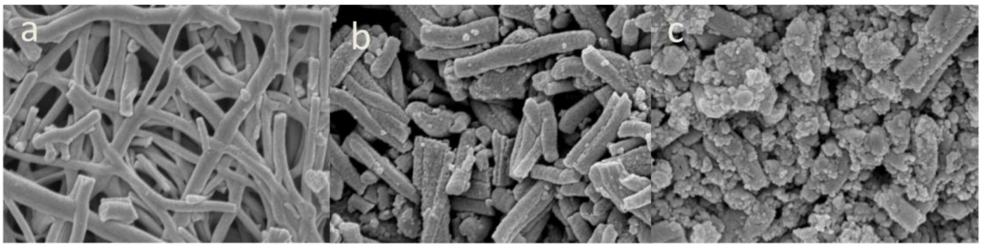

Figure s2. SEM images of samples with carbonization temperature of (a) 700 °C, (b) 900 °C and 1000 °C (c).

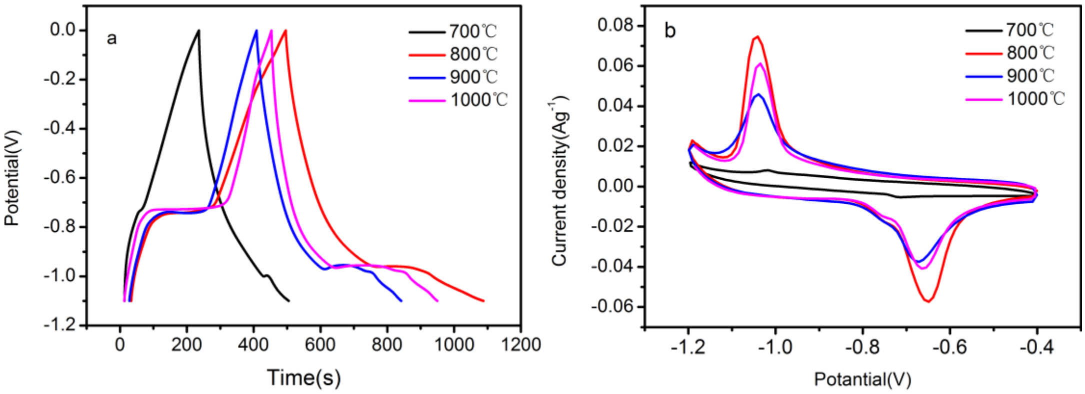

Figure s3. (a) GCD curves of different carbonization temperature samples at the current density of 1 A g^{-1}; (b) CV curves for different carbonization temperature samples at a scan rate of 10 mV s^{-1}.

References

1. P. Simon, and Y. Gogotsi. *Acc Chem Res.*, 46 (2013) 1094.
2. J.M. Wang, Z.K. Wang, M. Li and C.C. Zhang, *Advanced Energy Materials*, 8 (2018) 1701688.
3. R. Guo, J. Li,Y.F. Jia and F. Xin, *Journal of Materials Chemistry A*, 7 (2019) 8.
4. E. Ekrami, and F. Dadashian, M. Soleimani, *Fibers & Polymers*, 15 (2014) 1855.
5. A.R. Duggal and L.M. Levinson, *Journal of Applied Physics*, 82 (1997) 5532.
6. G. Zhang, X. Xiao, B. Li and P. Gu, *Journal of Materials Chemistry A*, 5 (2017) 8155.
7. W.Si, J. Zhou, S. Zhang, S.J. Zhang, W. Xing and S.P. Zhuo. *Electrochimica Acta*, 107 (2013) 397.

8. S.Y. Lu, M. Jin,Y. Zhang and Y.B. Niu, *Advanced Energy Materials*, 8 (2018) 1702545.
9. H. Liang, D.C. Chen, Y. Ding, F. Shi, Z.L. Wang and M.L. Liu, *Nano Letters*, 13 (2013) 3135.
10. M.M. Xia,Y.Y. Zhu and Q.T. Sun, *Chemical Communications*, 51 (2015) 8789.
11. Y. Wang,Y.L. Zheng,Q.Y. Zhang and L. Zuo, *Carbon*, 111 (2016) 419.
12. D. Gao, L.L. Wang, C.X. Wang and Q.F. Wei, *Fibers & Polymers*, 16 (2015) 421.
13. G. Bhuvanalogini, N. Murugananthem, V. Shobana and A. Subramania, *Journal of Solid State Electrochemistry*, 18 (2014) 2387.
14. R. Guo, J. Li and Y.F.Jia, *Journal of Materials Chemistry A*, 7 (2019) 353.
15. J.X. Ma, J. Li.R. Guo, H. Xu, F. Shi, .Q. Dang, Z.H. Liu, J. Sun and Z.B. Lei, *Journal of Power Sources*,4 (2019)101.
16. D.G. Lee, , H.K. Ji and B.H. Kim, *Electrochimica Acta*, 200 (2016) 174.
17. V.D. Nithya, and N.S. Arul, *Journal of Power Sources*, 327 (2016) 297.
18. C. Guan, J. Liu, Y. Wang, L. Z.Fan,Z. Fan, Z. Shen,H. Zhang and J. Wang, *Acs Nano*, 9 (2015) 5198.
19. G. Cao,W. Zhao, Y.T. Hu and Q.Q. Ke, *Advanced Energy Materials*, 6 (2016) 1601034.
20. X.F. Lu, X.Y. Chen and W. Zhou, *Acs Appl Mater Interfaces*, 7 (2015) 14843.
21. N.C. Abeykoon, J.S. Bonso and J.P. Ferraris, *Rsc Advances*, 5 (2015)19865.
22. Kai Li, W.B. Zhang, Z.Y. Zhao, Y. Zhao, X.W. Chen and L.B. Kong, *Nano*, 13 (2018) 604.
23. H.l. Wang , Z.w. Xu, A. Kohandehghan, Z. Li, K. Cui, X.h. Tan, T.J. Stephenson,C. K. King'ondu, C. M. B. Holt, B.C. Olsen, J. K. Tak, D. Harfield , A. O. Anyia and D. Mitlin, *Acs Nano*, 7 (2013) 5131.
24. L.z. Lin, Y.G. Yao, M. Yoshioka and N. Shiraishi, *Carbohydrate Polymers*, 57 (2004) 123.
25. B. N. Kuznetsov, V. I. Sharypov, N. V. Chesnokov, N. G. Beregovtsova, S. V. Baryshnikov, A. V. Lavrenov, A. V. Vosmerikov and V. E. Agabekov, *Kinetics & Catalysis*, 56 (2015) 434.
26. X. Jiang, C. Liu, G.F. Shi, G.Y. Wang, Z. Wang, S.M. Jia, Y.C. Dong, P. Mishra, H.Q. Tian and Y.R. Liu, *RSC Advances*, 9 (2019) 23324.
27. G.H. He, Y.H. Song, S.L. Chen and L. Wang, *Journal of Materials Science*, 53 (2018) 9721.
28. K. Li, W.B. Zhang, Z.Y. Zhao, Y. Zhao, X.W. Chen and .B. Kong, *Nano*, 7 (2018) 1850091.
29. R.Z. Li, Y. Wang, C. Zhou, C. Wang, X. Ba, Y. Li, X. Huang and J. Liu, *Advanced Functional Materials*, 25 (2015) 5384.
30. B. Lobato, L. Suárez, L. Guardia and T. A. Centeno, *Carbon*, 122 (2017) 434.
31. T. Chau and K.Vibha, *Journal of Power Sources*, 235 (2013)289.
32. J. Gamby, P.L.Taberna,P.Simon, J.F. Fauvarque and M.C.hesneau, *Journal of Power Sources*, 101 (2001) 109.
33. K. Song and Y. Lee, *Nanotechnology*, 23 (2012) 505401.
34. K. Song, Y. Lee, M.R. Jo., K.M.Nam and Y.M. Kan, Nanotechnology, 23(2012) 505401.
35. Liu, Y.L. and C.L. Xie, *Journal of Jinan University*, 18 (2010) 2073.
36. C. Lu, Y.H. Huang, Y.J. Wu, J. Li and J.P. Cheng, *Journal of Power Sources*, 394 (2018) 9.
37. C. Guan, W. Zhao, Y. Hu, Q.Q. Ke, X. Li, H. Zhang and J. Wang, *Adv. Energy Mater*, 25 (2016) 1601034.
38. L. Hao, X. Li and L. Zhi, *Advanced Materials*, 25 (2013) 3899.
39. G. Cheng, X. Zhang and Simmons, *Energy & Environmental Science*, 8 (2015) 436.
40. J.J. R. JANSEN and V. Bekkum, *Carbon*, 33 (1995)1021.
41. G. C. Allen, M.T. Curtis, A.J. Hooper and Philip M. Tucker, *Journal of the Chemical Society Dalton Transactions*, 14 (1974) 1525.
42. D. Brion, *Applications of Surface Science*, 5 (1980) 133.
43. X.F. Lu, X.Y. Chen and Wen Zhou, *Acs Appl Mater Interfaces*, 7 (2015) 14843.
44. W. Wei, S.B. Yang, H.X. Zhou, I. Lieberwirth, X.L. Fengand and K. Müllen, *Advanced Materials*, 25 (2013) 2909.
45. M. Zhou, F. Pu, Z. Wang and S.Y. Guan, *Carbon*, 68 (2014) 185.

46. E.R.Ezeigwea, M.T.T. Tana, P.S.Khiewa and C.W.Siong, *Ceramics International*, 41 (2015) 715.
47. N. C. Abeykoon, J. S. Bonso, J. P. Ferraris, *RSC Advances*, 5 (2012)16594.